Control of Lateral Composition Distribution in Graded Films of Soluble Solid Systems $A_{1-x}B_x$ by Partitioned Dual-Beam Pulsed Laser Deposition

Joe Sakai [1,*], **José Manuel Caicedo Roque [1]**, **Pablo Vales-Castro [1]**, **Jessica Padilla-Pantoja [1]**, **Guillaume Sauthier [1]**, **Gustau Catalan [1,2]** and **José Santiso [1]**

[1] Institut Català de Nanociència i Nanotecnologia (ICN2), ICN2 Building, UAB Campus, 08193 Bellaterra, Catalonia, Spain; jose.caicedo@icn2.cat (J.M.C.R.); pablo.vales@icn2.cat (P.V.-C.); jessica.padilla@icn2.cat (J.P.-P.); guillaume.sauthier@icn2.cat (G.S.); gustau.catalan@icn2.cat (G.C.); jose.santiso@icn2.cat (J.S.)

[2] Institució Catalana de Recerca i Estudis Avançats (ICREA), 08010 Barcelona, Catalonia, Spain

* Correspondence: jo.sakai@icn2.cat

Abstract: Lateral compositionally-graded thin films are powerful media for the observation of phase boundaries as well as for high-throughput materials exploration. We herein propose a method to prepare epitaxial lateral compositionally-graded films using a dual-beam pulsed laser deposition (PLD) method with two targets separated by a partition. Tuning the ambient pressure and the partition—substrate gap makes it possible to control of the gradient length of the deposits at the small sizes (≤ 10 mm) suitable for commercial oxide single crystal substrates. A simple Monte Carlo simulation qualitatively reproduced the characteristic features of the lateral thickness distribution. To demonstrate this method, we prepared $(1-x)PbTiO_3$—$xPbZrO_3$ and $(1-x)LaMnO_3$—$xLa_{0.6}Sr_{0.4}MnO_3$ films with lateral composition gradient widths of 10 and 1 mm, respectively, with the partitioned dual PLD.

Keywords: pulsed laser deposition; compositionally-graded film; morphotropic phase boundary; Monte Carlo method; piezoelectric material; perovskite type manganite

---

1. Introduction

In some soluble solid systems, represented as $A_{1-x}B_x$, one may find multiple phases with different crystallographic structures by varying the mixture ratio x from 0 to 1. Different crystalline phases separated by the morphotropic phase boundary (MPB) often correspond to remarkably different physical properties such as conductivity, magnetism, and piezoelectricity. Moreover, The MPB in some systems are known to be accompanied by enhanced dielectric, piezoelectric, or magnetic properties, which are expected to be, or have already been, applied to devices and commercial products. The outstanding physical properties at a MPB were first observed in the huge electromechanical coupling constant of $Pb(Zr,Ti)O_3$ (PZT) [1,2]. After this discovery, materials such as relaxor ferroelectric $Pb(Mg_{1/3}Nb_{2/3})O_3$–$PbTiO_3$ (PMN-PT) [3] and lead-free ferroelectrics $(Bi_{1/2}Na_{1/2})TiO_3$–$BaTiO_3$ (BNT-BT) [4] were developed as the result of the exploration of materials with MPB. Not only in ferroelectric, but also in magnetic materials, has the enhancement of physical properties at the MPB been reported [5]. The mechanism of the enhanced properties at the MPBs, which may depend on the material systems, is still the subject of research [6–8]. Therefore, understanding these MPBs in functional materials is essential from a scientific viewpoint and for application. In this respect, it is a popular theme of physics to nanoscopically observe the behavior of materials very near the MPB, where the lattice or the magnetic/dipole moments in one phase may be affected by the presence of the other.

Epitaxial films with lateral compositional gradients are well suited for the spatial observation of phase boundaries. A lateral compositionally-graded film, also referred to as a composition-spread film, is useful also as a combinatorial library [9] that enables high-throughput exploration of materials [10,11].

A popular method for preparing lateral, compositionally-graded films by pulsed laser deposition (PLD) is that multiple targets are sequentially irradiated with a single laser beam [12]. The alternate, wedgelike, submonolayer deposition of each material through a motor-driven shadowing mask enhances the precision of the spatial control of the composition (Figure 1a) [13]. Examples of lateral, compositionally-graded films prepared with masked sequential PLD include $(1-x)LaMnO_3$—$xSrMnO_3$ films [3,14], $(1-x)BaTiO_3$—$xSrTiO_3$ films [4,15], $(1-x)BiFeO_3$—$xGaFeO_3$ films [16], and $(1-x)BaTiO_3$—$x[Bi(Mg_{2/3}Nb_{1/3})O_3]$ films [17]. This method is advantageous in the preciseness of the design of lateral compositional evolution. On the other hand, the intermixing of species from different targets is allowed to occur only on the substrate surface. A substrate temperature of several-hundred degrees Celsius may not guarantee sufficient solid state diffusivity for the required high homogeneity of the material. This method tends to produce abrupt stoichiometry steps between each adjacent composition. It should also be noted that the sequential growth strategy inherently causes a low deposition rate, i.e., half or less than in standard PLD processes, hindering direct comparisons of the results.
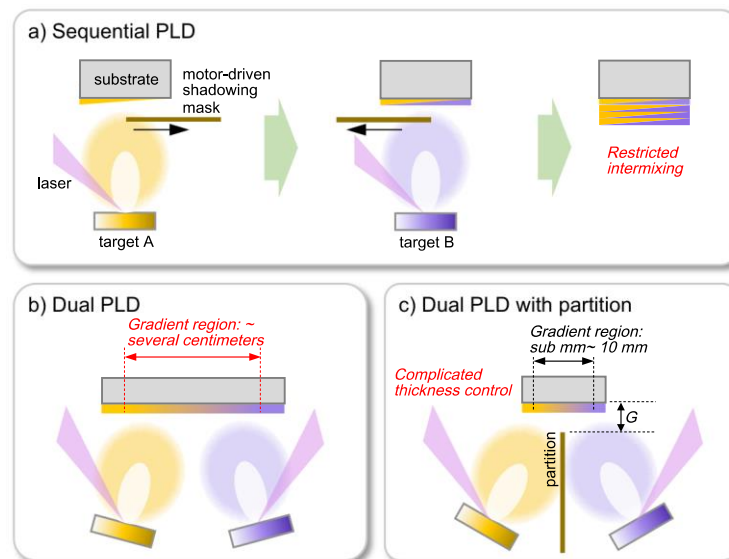

Figure 1. Schematics of PLD setups for fabricating compositionally-graded films. (**a**) Sequential single-beam PLD. (**b**) Simultaneous dual-beam PLD without partition. (**c**) Partitioned, simultaneous dual-beam PLD.

In the present work, we adopt a dual-beam PLD scheme, in which two laser beams are shed onto two targets simultaneously (Figure 1b,c). Pioneering examples of simultaneous dual PLD for obtaining films with homogenous composition include $YBa_2Cu_3O_{7-\delta}$ films made from YBa_2O_x and CuO targets [18] and cobalt-doping on $BaTiO_3$ films [19]. The dual-beam PLD scheme was then adopted to achieve a lateral, compositionally-graded film of $(1-x)BaTiO_3$—$xSrTiO_3$ [20]. Perfect synchronicity in the ejection of the species from both targets can be regarded as an advantage of the simultaneous dual-PLD method over sequential PLD. The mixing of the species may start in the space before arrival at the substrate, thereby taking advantage of the higher reaction energy of the particles. The resulting films, therefore, have a more continuous compositional gradient.

On the other hand, controlling the lateral composition distribution on the substrate is more complicated in this method, since the composition footprint on the substrate is governed by the overlap of the axial distribution of both plumes, which may be quite broad if no additional geometrical constraints are interposed. Some ablation processes for obtaining laterally graded films intentionally

utilize the thickness decay typical in PLD (Figure 1b) [12,21]. This is a smart strategy, but the scale of decay (several centimeters) requires the usage of multiple small substrates or a large-sized substrate such as a silicon (Si) wafer or a glass plate for such a laterally graded film [12,20,21]. To obtain epitaxial oxide films, there is a strong demand for oxide single-crystal substrates, which are often of sizes of 10 to 15 mm at largest, meaning that the region of decay in PLD is too large to be used for such substrates.

A metal sheet between the two targets (a partition) with adjustable length and position is expected to help control the areal region of the reaction, and to give rise to a composition gradient in a relatively narrow region, i.e., of submillimeter to 10 mm (Figure 1c). A sharp gradient is advantageous for microscopic or nanoscopic observations of a phase boundary by means of scanning electron microscopy (SEM) or scanning probe microscopy (SPM). The purpose of these observations is to clarify in detail the spatial metamorphoses in topographical or physical properties from one phase to the other. For this, it is required that two phases on both sides of the boundary are confined to a scanning area. A sharp composition gradient is demanded in the sample for such observations. No method has been published describing how to grow graded composition films with uniform thickness by the PLD with a partition, neither experimentally nor theoretically predicted.

The aim of the present study is to establish the basic techniques for dual-beam PLD with a partition. First, we examined the film thickness distribution obtained by the partitioned PLD with a single target. In order to understand the factors that bring about the characteristic film thickness distribution, we performed a simplified Monte Carlo simulation on the trajectories of the ejected particles. The Monte Carlo method has been widely utilized to successfully reproduce the distribution of deposits on the substrate in PLD processes [22–25]. Finally, we applied this methodology to the preparation of graded films of two representative perovskite families, PZT and $La_{1-y}Sr_yMnO_3$ (LSMO), as the prototypes of multiphase systems. The former is supposed to include tetragonal—rhombohedral and rhombohedral—orthorhombic phase boundaries [1,2], whereas the latter should contain a paramagnetic insulator—ferromagnetic metal phase boundary [26,27].

2. Experiments and Simulation

2.1. Deposition Equipment

In our equipment customized for dual-beam PLD (Surface Tech, Hückelhoven, Germany), a laser beam from an excimer laser (COMPex 102, KrF gas, wavelength of 248 nm, Lambda Physik, Göttingen, Germany) is split into two beams by a half mirror, each of which is focused on each individual target. In order to balance the deposition rates from the two targets, an attenuator is inserted in each of the two optical paths.

The two target holders are placed side by side, can be tilted at an arbitrary angle, and have a mechanism of in-plane rotation. In the present experiments, both targets were tilted so that the plumes were directed toward the center of the substrate, which was placed 50 mm apart from both target surfaces. A partition, either a 0.3 mm-thick copper or 0.1 mm-thick stainless-steel plate, was installed between two targets, leaving a gap (G) between the substrate surface and the end of the partition, as depicted in Figure 1c. This variable gap is intended to control the spatial region where the mixing between ablated species from the two targets is produced. The laser spots on both targets were about 10 mm apart from the partition.

2.2. Characterization

The lateral distribution of deposits on the samples in single-target experiments (Section 3.1) was evaluated with line analyses of energy-dispersive x-ray (EDX) spectroscopy (X-Max, Oxford Instruments, High Wycombe, UK). In the EDX system, the observable region is about 3 mm-long at its largest, and non-uniformity of the sensitivity occurs at such a magnification. Therefore, analysis of a sample (5 to 10 mm-long) was done by observing multiple regions in series, and finally connecting the profiles to obtain a whole profile. Each line profile was calibrated with the profile of a Si standard sample.

For a compositionally-graded film with a wide gradient region (Section 4.1), the surface morphology, the composition, and the crystalline structure were characterized with scanning electron microscopy (SEM), X-ray photoelectron spectroscopy (XPS), and X-ray diffraction (XRD) techniques, respectively, at 10 points with an increment of 1 mm on a line along the composition gradient direction. The increment of 1 mm was chosen because the X-ray spot widths of the XPS and XRD equipments is sub-millimeter size. SEM (Quanta 650 FEG, FEI, Hillsboro, OR, USA) images were observed in a secondary electrons (SE) mode with an acceleration energy of 5.0 kV. XPS measurements were performed at room temperature (RT) with a hemispherical analyzer (PHOIBOS 150, SPECS, Berlin, Germany) at a base pressure of 4×10^{-10} Torr. Monochromatic Al Kα radiation (1486.86 eV) was used as the excitation source with a power of 300 W. The x-ray spot on the sample surface in a size of 3.5 mm $\times$ 0.5 mm is defined by a quartz crystal that plays the roles of a monochromator and a focusing device. Standard XRD was carried out at RT in a 2θ–ω configuration using a diffractometer with four-circle goniometer (X'pert PRO-MRD, Malvern-PANalytical, Almelo, The Netherlands). The measurements were performed using Cu Kα radiation source (1.5406 Å) with a Ni filter for cutting out Kβ radiation, and primary optics consisting of a parabolic mirror with a small divergent slit (1/8°) and the smaller mask (2 mm) to reduce the irradiated area in sub-millimeter size. To confirm the local FE properties, piezoresponse force microscopy (PFM) experiments were carried out at selected regions on the sample surface using a scanning probe microscopy system (MFP-3D Classic, Asylum Research, Santa Barbara, CA, USA) in dual-AC resonance tracking mode. The probe (PPP-EFM, Nanosensors, Neuchâtel, Switzerland) was made of Si and the tip coated with Pt/Ir. The spring constant of the cantilever was 2.8 N/m, and its resonance frequency in air was 68 kHz. AC voltage of an amplitude of 1 V was applied to drive the probe.

2.3. Simulation

The trajectories of particles ablated from a single target to reach the substrate surface under various conditions (pressure p_{O2} and gap G) were simulated by a Monte Carlo method with a simple model. See Supplementary Material for detailed description of the model and the coordinate system used for the calculation [22–24,28,29].

3. Single Target Ablation Experiment and Simulation

3.1. Experiment

Before putting the partitioned dual-PLD into practice, it was essential for us to check how the ablated species were affected by the partition. In order to examine the thickness distribution on the substrate, we performed a starting experiment in which a single target was placed on a side of the partition, and ablated by a laser beam under various conditions (oxygen pressure p_{O2} and substrate—partition gap G). In each deposition, a CeO_2 target was irradiated by 5000 pulses of laser shots at a frequency of 8 Hz. The laser energy and the fluence on the target surface was 50 mJ/pulse and 1.5 J/cm^2, respectively. The p_{O2} was varied between 10 and 100 mTorr, whereas G was 1, 2, or 4 mm. Si was used as the substrate, which was intentionally not heated during the ablation.

Figure 2a shows scanned images of CeO_2/Si samples deposited under various conditions. The visible transparency of CeO_2 and gradual evolution of thickness along one direction caused colorful interference fringes. As the thickness increased from left to right, a dark line appeared first, which turns to light blue, yellow, and finally pink-colored bands. Thus, the spread of the color bands is a qualitative indication of the thickness change. As can be seen in the images, the lateral thickness distribution varies as a function of the ambient pressure and the gap. Larger G brings about gentler thickness distribution under constant p_{O2}, as does higher p_{O2} with constant G. The increase in the gap allows the ablated particles that pass through it to have more opportunities to collide with ambient oxygen molecules, resulting in a higher lateral distribution beyond the partition and, consequently,

a wider thickness gradient. Likewise, a higher deposition pressure increases for the probability of collisions, again resulting in enhanced lateral scattering of the particles and a wider gradient.

In order to obtain the quantitative spatial distribution of the amount of material deposited, the signal intensity of Ce was evaluated over the entire width of the samples by EDX line analyses, as shown in Figure 2b–d. Besides the obvious lowering in overall material transfer under higher p_{O2}, which caused the expected reduction of deposition rate, they clarify the trends mentioned above. In detail, two common features can be found in the Ce distribution (proportional to film thickness distribution) profiles, namely, (1) a gentle gradient on the target side (right-hand side in the panels), and (2) a steep gradient on the opposite side. A steep gradient obviously corresponds to Ce species that diffused through the gap. However, the origin of the gentle slope on the target side remained mysterious at this stage, which motivated us to carry out a simulation.
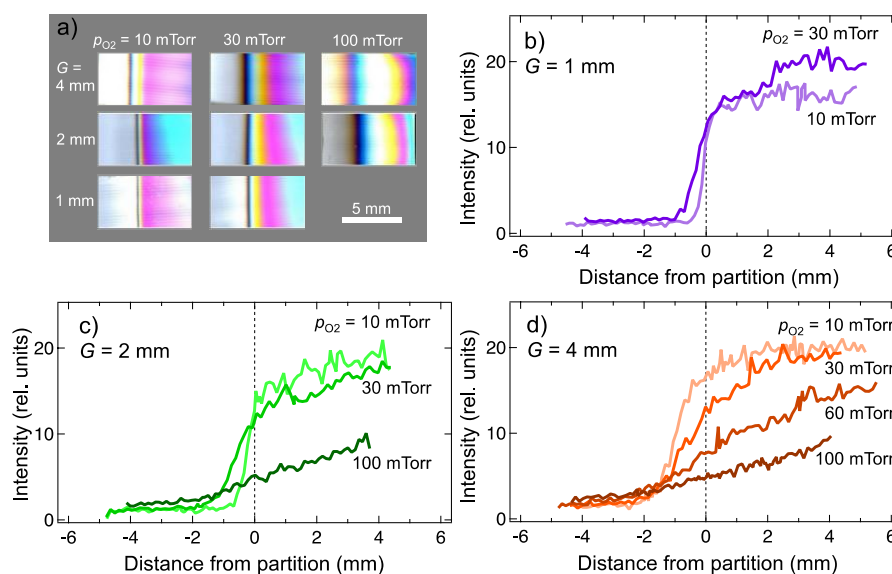

Figure 2. (**a**) Optical-scanner images of CeO$_2$/Si samples prepared by partitioned single-target PLD with various gaps and oxygen ambient pressures. In all the images in the figure the right hand-side corresponds to the target side during deposition. The center in the horizontal direction of each image corresponds to the partition position during deposition. (**b**)–(**d**) EDX signal intensity profile of Ce as functions of position on the CeO$_2$/Si samples. The partition–substrate gap is 1 mm (**b**), 2 mm (**c**) and 4 mm (**d**).

3.2. Simulation

Figure 3a,b show the simulation results of the deposition profiles of CeO$_2$ ablated under various oxygen pressure p_{O2} and partition—substrate gap G, respectively. The features on the experimental Ce distribution such as steep and gentle gradients, as well as the pressure and gap dependency, were qualitatively reproduced, suggesting that the use of such 2D model (as a simplification of a more realistic, but computationally complex, 3D model) does not significantly affect the simulation results. In Figure 3c, the simulated deposition profiles were compared for a wider area between cases with ($G = 4$ mm) and without ($G = 50$ mm) a partition. Here, the angle measured from the plume axis, Θ, was adopted as the horizontal axis value instead of X (see Figure S1). It was revealed, unexpectedly, that the maximum of the deposition profiles is not on the plume axis ($\Theta = 0°$) but is shifted towards the target side by $\Theta_s \sim 10°$. The shift does not occur when the substrate is in parallel with the target surface. Therefore, the simulation clarified that the inclination of the substrate with respect to the target surface is the origin of the shift and the gentle gradient on the target side. The shifted profile is probably ruled by the balance between the angular dependence ($\cos^N \Theta$ decay from the plume axis) and the slight increase in deposition rate at shorter distance from the laser spot on the target to the substrate position.

In order to find an analytical expression to account for the step change in the angular distribution of ejected species caused by the partition, a classical error function term was introduced. For rough evaluation of the degree of diffusion beyond the partition, we fitted the experimental Ce deposit profiles *I* with the following equation:

$$I = \frac{a}{2} \cos^N(\Theta - \Theta_s) \cdot \mathrm{erf}\frac{X - X_0}{\sqrt{2}\omega} + d, \tag{1}$$

where a, N, Θ_s, X_0, ω, and d are the fitting parameters. The $\cos^N(\Theta - \Theta_s)$ corresponds to the distribution in the case of no partition, and d the background. Instead of constructing a highly sophisticated model based on the realistic mechanism of perturbation caused by the partition (diffusion beyond the gap and loss due to the collision with the partition), the error function was adopted because its shape seems to reproduce the actual perturbation. The ω values, which can be regarded as approximate indicators of the diffusion lengths beyond the partition, are extracted from the fitting and 3D-plotted in Figure 3d as functions of p_{O2} and G. It should be noted that only in a narrow region of G and p_{O2} can the two types of gradient, before and after the partition, be comparable, producing a smooth overall distribution across the film. For the general deposition of compositionally-graded films with a partition, proper parameters p_{O2} and G should be chosen considering both the required gradient width and the ambient pressure suitable for the growth of high-quality films of the material.
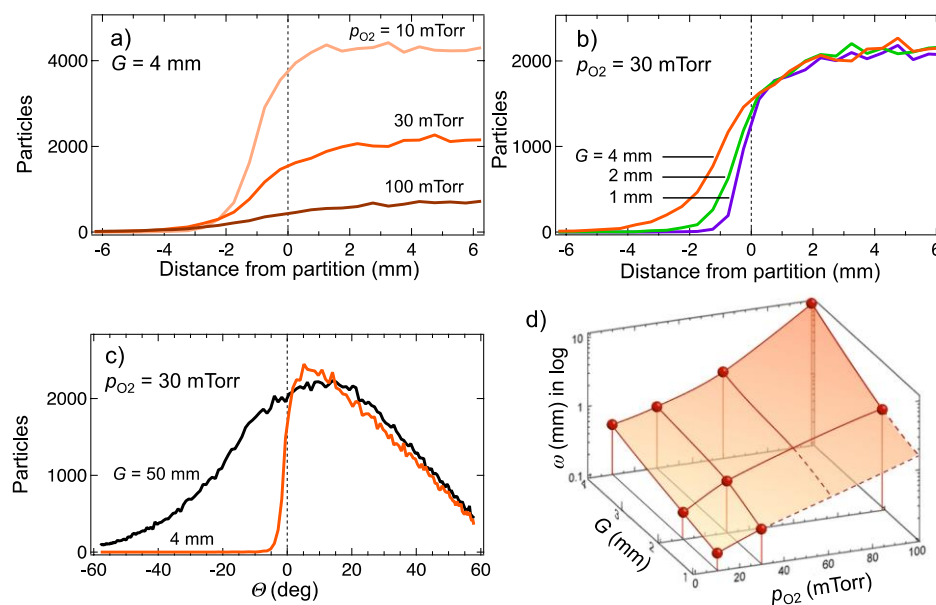

Figure 3. (**a**)–(**c**) Simulated distribution of particles ablated under various oxygen pressures and gaps. (**a**) Pressure dependency with a fixed gap of 4 mm. (**b**) Gap dependency with a fixed pressure of 30 mTorr. (**c**) Comparison between cases with and without the partition. $G = 50$ mm corresponds to the case without the partition. (**d**) 3D-plot of ω values, extracted from fitting to experimental Ce distribution (Figure 2), as a function of gap and oxygen pressure. Red balls represent the extracted values. Curved lines and filling color are guides to the eyes.

4. Deposition of Compositionally-Graded Films

4.1. (1−x)PbTiO₃—xPbZrO₃

A typical example of A_xB_{1-x} that contains phase boundaries is PZT, a solid solution of tetragonal ferroelectric (FE) PbTiO₃ (PTO) and orthorhombic antiferroelectric (AFE) PbZrO₃ (PZO). Focusing on the RT characteristics for the x range from 0 to 1, one finds a MPB of around $x = 0.5$, where the crystalline structure switches from tetragonal to rhombohedral via a monoclinic bridging phase,

and then a FE–AFE phase boundary around $x = 0.9$, where the structure changes to orthorhombic [1,2]. The PZT compound with a composition within the MPB region is known to show an extraordinary electromechanical coupling factor, which makes the material of this composition utilized in a wide range of applications as a piezoelectric material [1].

Here, a $(1-x)$PTO—xPZO lateral compositionally graded film was prepared on a $SrTiO_3$ (001) substrate of 5 mm × 10 mm in dimension with a bottom electrode layer of $La_{0.6}Sr_{0.4}MnO_3$ (LSMO; $y = 0.4$). Lead-excess $Pb_{1.1}TiO_3$ and $Pb_{1.1}ZrO_3$ polycrystalline targets were used for preparing the graded PZT film, as typically performed for Pb-containing compounds which tend to loose Pb during deposition due to the high volatility of PbO. The substrate temperature was 650 °C for deposition of LSMO and 550 °C for graded PZT. The oxygen pressure was maintained at 100 mTorr during deposition of both layers. This high oxygen pressure is essential for preventing the re-evaporation of Pb in PLD of Pb-containing compounds. The partition—substrate gap was set to 5 mm to realize a broad composition change over the entire substrate area (10 mm in length). The laser energy and the fluence on the target surface were 50 mJ/pulse and 2 J/cm²/pulse, respectively. The thickness of each layer estimated with X-ray reflectivity was about 50 nm for LSMO and about 80 nm for graded PZT layers.

Figure 4a shows XRD 2θ–ω scan profiles around $(002)_c$ peaks taken at 10 points with 1 mm increment on the $(1-x)$PTO—xPZO/LSMO/STO (001) sample, where the subscript c denotes indexing corresponding to pseudo-cubic structure. Scans for a wider 2θ range of 10°–80° (not shown) confirmed that the graded PZT layer, as well as the LSMO, were single-oriented, with no secondary phases or other orientation. The PZT $(002)_c$ peak angles gradually evolved with respect to the spatial position, in correspondence to the varying composition. The PZT $(002)_c$ peaks were sharper on the PZO side than on the PTO side.

Similarly, the surface morphology was observed by SEM (Figure 4b), and the composition of the PZT layer was evaluated by XPS (Figure 4c), at the same 10 points where XRD was performed. The Zr ratio in the B site, $[Zr]/([Zr] + [Ti])$ $(= x)$, evolved continuously from 17% to 96%. A comparison of the morphology and the composition revealed that the surface was flat and continuous in the region $x < 0.5$, but had more defects at higher x, showing a granular texture at $x > 0.9$. A large mismatch between the PZO and LSMO layers probably caused the full relaxation and granulation of the PZT layer.

The interplanar lattice spacing of the PZT layer at the 10 points, calculated from the 2θ angles of PZT $(002)_c$ diffraction peaks, are plotted as a function of Zr ratio x in Figure 4d. For comparison, in the same figure are shown the lattice parameters of PZT materials with various x reported in two previous papers, one on bulk samples [30] and the other on films grown on $SrTiO_3$ (001) by metal organic chemical vapor deposition (MOCVD) [31]. The out-of-plane lattice parameters of the present film were consistent with MOCVD films in compositions of PZO side $(x > 0.5)$, but were shorter than c-axis length of bulk and MOCVD films in which the structure is supposed to be tetragonal $(x < 0.5)$. The LSMO layer underneath could play a role in weakening the tetragonality. It could be that the PZT $x < 0.5$ microstructure consists of an intimate mixture of c- and a-axis nanodomains not resolved by XRD, which measures an average value with a quite broad peak, although the precise mechanism is not clear.

PFM observation was performed on multiple regions of the $(1-x)$PTO—xPZO/LSMO/STO (001) sample. In a region 5.0 mm from the PZO-side edge, corresponding to Zr ratio x of 0.75, the polarization—field scans (not shown) showed decent FE hysteresis loops. The evolution of phase was confirmed in the polarized areas (Figure 4e(ii)), indicating an upwards out-of-plane net polarization, which was easily switched downwards. Thus, we concluded that this region was FE with a good functionality. On the other hand, in a region 1.5 mm from the PZO-side edge, corresponding to x of 0.94, there seemed to be a mixture of domains that were FE and others that might be AFE (Figure 4e(i)). Although the results in this region were not conclusive, the region might be close to the phase boundary composition and thus might still contain FE domains.
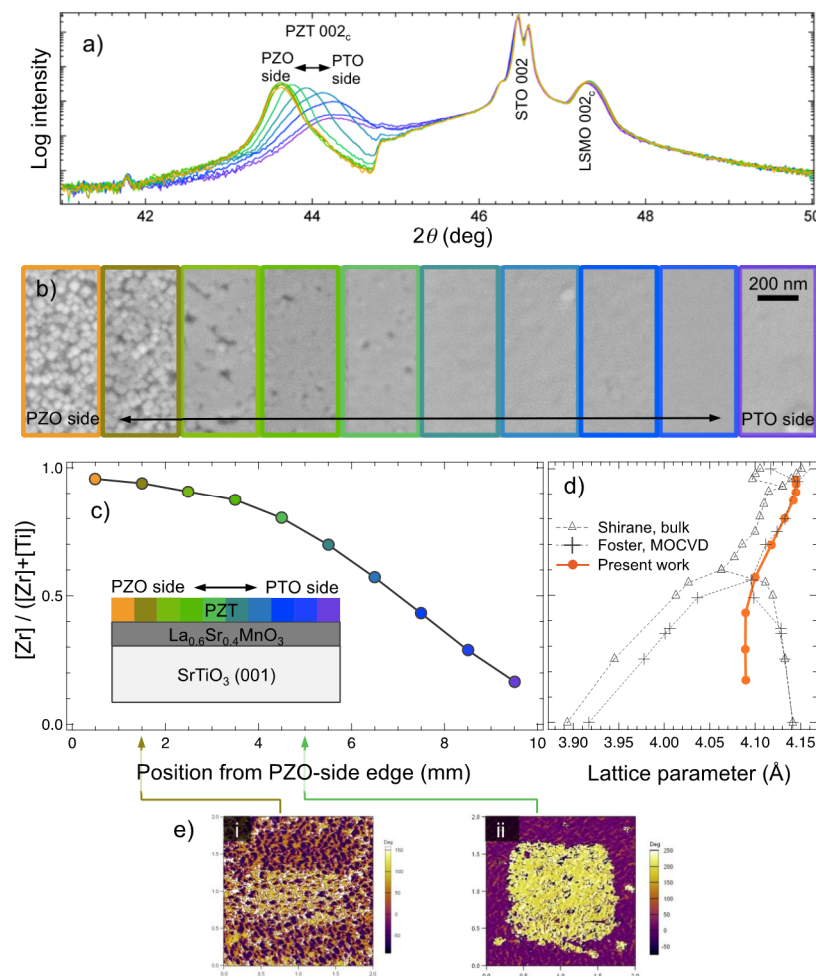
Figure 4. XRD 2θ–ω profiles (**a**), SEM images (**b**), and Zr ratio [Zr]/([Zr] + [Ti]) evaluated by XPS (**c**), at 10 points on a $(1-x)$PbTiO$_3$—xPbZrO$_3$ laterally composition gradient film. Colors of lines in (**a**), of frames in (**b**), and of symbols in (**c**) are corresponding with each other and representing the position on the film, as illustrated in the inset of (**c**). (**d**) Relationship of interplanar lattice spacing calculated from the 2θ angles of PZT (002)$_c$ diffraction peaks (Figure 4a) and Zr ratio (Figure 4c). Reported values of lattice parameters of PZT materials with various compositions in bulk samples [30] and on films grown on SrTiO$_3$ (001) by metal organic chemical vapor deposition (MOCVD) [31], are also shown for comparison. (**e**) PFM phase images after polarization at points 1.5 mm (i) and 5.0 mm (ii) from PZO-side edge. The observation area for each is 2 μm × 2 μm.

4.2. $(1-x)$LaMnO$_3$—xLa$_{0.6}$Sr$_{0.4}$MnO$_3$

As another typical example of a solid solution system including a phase boundary, we chose La$_{1-y}$Sr$_y$MnO$_3$ (LSMO), whose rich phase diagram contains an antiferromagnetic insulator, paramagnetic insulator and ferromagnetic metal phases. A previous study on single crystals with various Sr substitution level y has revealed that a paramagnetic insulator—ferromagnetic metal phase boundary exists at around $y = 0.2$ at RT (~25 °C) [26]. LSMO in ferromagnetic metallic phase is known to show a giant magnetoresistance effect, and is actively studied for application to magnetic random access memory (MRAM) devices [27].

We attempted to fabricate a LSMO film with laterally-graded Sr level y from 0 (LMO) to 0.4. Commonly used oxygen pressures for PLD of LSMO are on the order of 100 mTorr [32,33], although some groups report successful PLD of high quality LSMO films with a much lower oxygen pressure, i.e., $\leq 10^{-4}$ Torr [34,35]. The p_{O2} could cause a distinct effect on both magnetic and electronic properties in LMO thin films [36]. For the present LSMO graded film, p_{O2} and G were set at 10 mTorr and 1 mm,

respectively, targeting a narrow gradient width. Substrate temperature, laser energy, and fluence on the target surface were 650 °C, 44 mJ, and 2 J/cm^2, respectively. The nominal thickness of the graded LSMO layer was estimated to be about 150 nm. An EDX line analysis was performed to obtain the composition profile. For this reason, attention was paid to the selection of the substrate material. Since the observation depth of EDX is on the order of 1 μm, it is inevitable to catch the signals from the substrate under the 150 nm-thick film. Thus, a NdGaO$_3$ (110) substrate was selected due to the advantage that signals of the elements in it do not hide either La or Sr signals, in contrast to other perovskite-type substrates such as SrTiO$_3$, LaAlO$_3$, and (La,Sr)(Al,Ta)O$_3$. Part of the graded LSMO layer was coated with Pd to ensure conductivity for the EDX analysis. Here again, Pd was selected because its signals do not overlap with La and Sr.

The calibrated EDX signals of La, Sr, and Mn are shown in Figure 5c. A region at 2.0 to 2.7 mm from the LMO-side edge is accompanied by La and Mn signals stronger than the other part, suggesting a larger thickness. The region is identical with the bright colored band found in the optical image (Figure 5a). La/Mn and Sr/Mn intensity ratios (Figure 5d) show that the main changes of the amounts of La and Sr take place in the same region, i.e., approximately 1.8 to 2.8 mm from LMO-side edge. In contrast to the PZT case with p_{O2} of 100 mTorr and G of 5 mm (Section 4.1), a narrow composition gradient region of about 1 mm was achieved with low p_{O2} and small G, as expected.
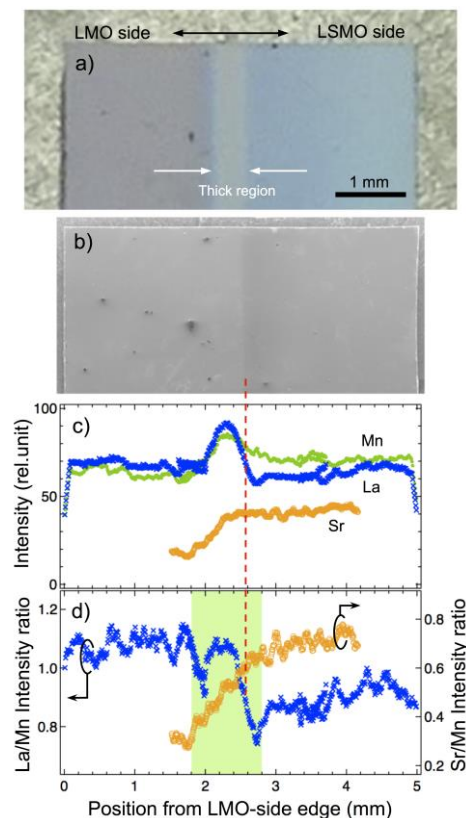

Figure 5. Optical image (**a**), SEM image (**b**), calibrated EDX signals of La, Sr, and Mn (**c**), and the EDX signals intensity ratio of La/Mn (crosses) and Sr/Mn (circles) (**d**) of a $(1-x)$LaMnO$_3$—xLa$_{0.6}$Sr$_{0.4}$MnO$_3$ film. All panels are aligned so that the horizontal position in the images and the horizontal axes values in the graphs correspond to each other. Dashed line represents the position of the contrast boundary in the SEM image (Figure 5b). Colored area in Figure 5d represents the supposed compositionally-graded region.

Two regions with different brightness, implying some different physical properties, are seen in the SEM image (Figure 5b). Although it is difficult to know the precise composition of the boundary, it lies within the composition graded region between LMO and LSMO ($y = 0.4$), as indicated with a dashed

line in Figure 5. This is consistent with the foreseen metal-insulating transition at RT that occurs when y crosses 0.2 [26]. Further local transport analyses are needed to confirm this assumption.

5. Conclusions

We propose a partitioned dual PLD method for fabricating lateral compositionally-graded films. The effects of two deposition parameters, namely the partition—substrate gap and the ambient pressure, on the film thickness distribution were experimentally investigated. A Monte Carlo simulation was performed in order to understand the characteristic features of the distribution. The predictions of the model are that the width of the gradient region is a monotonously increasing function of both the partition—substrate gap and the oxygen ambient pressure during deposition. These predictions were experimentally confirmed.

We obtained $(1-x)$PbTiO$_3$—xPbZrO$_3$ and $(1-x)$LaMnO$_3$—xLa$_{0.6}$Sr$_{0.4}$MnO$_3$ graded films of wide (~10 mm) and narrow (~1 mm) composition gradient widths, respectively. It is noteworthy that the method proposed here is currently the only one that achieves a composition gradient of as narrow as ~1 mm in a thin film. Both films maintained crystallographic coherence and a smooth compositional gradient across the intermixing region, but they also evidenced some limitations. In particular, the PZT graded film showed that the difference in lattice mismatch between the substrate/bottom electrode and the two compositional end-members resulted in one side of the film (the PbTiO$_3$ side) being much smoother and continuous while the other (PbZrO$_3$) is relaxed forming columnar grains. This stresses the importance of carefully choosing the film-substrate combination so that both sides of the phase diagram can be grown with good epitaxy. In contrast, the LSMO graded film showed good epitaxy at both ends, but the narrow gradient region was raised with respect to the rest of the film, indicating that thickness gradients can be harder to avoid when the gradient region is sharply confined.

The present deposition technique allows one to examine the composition dependency of various properties in a solution system A$_{1-x}$B$_x$ with a single sample, enhancing the throughput. Though each individual composition along the gradient exists only in a narrow part of the sample, scanning probe microscopy techniques make it possible to probe the properties at each composition separately. Provided that the aforementioned requirements (consistent lattice mismatch and homogeneous thickness) are met, one can draw the entire phase diagram of a given perovskite family with a single film. Since the present scheme is suitable for preparing epitaxial compositionally-graded films, it will speed up the exploration of not only the composition, but also the combination of the composition and epitaxial strain, which would be a key factor in the development of strain-driven devices.

Author Contributions: Conceptualization, funding acquisition, and reviewing draft, G.C. and J.S. (José Santiso); Development of methodology, J.M.C.R.; Performing films deposition, EDX and SEM analysis, simulation, and writing draft, J.S. (Joe Sakai); Performing XRD analysis, J.P.-P.; Performing XPS analysis, G.S.; Performing PFM observation, P.V.-C. All authors have read and agreed to the published version of the manuscript.

Conflicts of Interest: The authors declare no conflict of interest.

References

1. Jaffe, B.; Cook, W.R.; Jaffe, H. *Piezoelectric Ceramics*; Academic Press: London, UK, 1971.
2. Noheda, B.; Gonzalo, J.A.; Cross, L.E.; Guo, R.; Park, S.-E.; Cox, D.E.; Shirane, G. Tetragonal-to-monoclinic phase transition in a ferroelectric perovskite: The structure of $PbZr_{0.52}Ti_{0.48}O_3$. *Phys. Rev. B* **2000**, *61*, 8687–8695. [CrossRef]
3. Park, S.E.; Shrout, T.E. Ultrahigh strain and piezoelectric behavior in relaxor based ferroelectric single crystals. *J. Appl. Phys.* **1997**, *82*, 1804–1811. [CrossRef]
4. Takenaka, T.; Maruyama, K.; Sakata, K. $(Bi_{1/2}Na_{1/2})TiO_3$-$BaTiO_3$ system for lead-free piezoelectric ceramics. *Jpn. J. Appl. Phys.* **1991**, *30*, 2236–2239. [CrossRef]
5. Yang, S.; Bao, H.; Zhou, C.; Wang, Y.; Ren, X.; Matsushita, Y.; Katsuya, Y.; Tanaka, M.; Kobayashi, K.; Song, X.; et al. Large magnetostriction from morphotropic phase boundary in ferromagnets. *Phys. Rev. Lett.* **2010**, *104*, 197201. [CrossRef] [PubMed]
6. Zhang, N.; Yokota, H.; Glazer, A.M.; Keen, D.A.; Gorfman, S.; Thomas, P.A.; Rena, W.; Yeb, Z.G. Local-scale structures across the morphotropic phase boundary in $PbZr_{1−x}Ti_xO_3$. *IUCrJ* **2018**, *5*, 73–81. [CrossRef] [PubMed]
7. Fang, M.; Rajput, S.; Dai, Z.; Ji, Y.; Hao, Y.; Ren, X. Understanding the mechanism of thermal-stable high-performance piezoelectricity. *Acta Mater.* **2019**, *169*, 155–161. [CrossRef]
8. Gao, J.; Hu, X.; Wang, Y.; Liu, Y.; Zhang, L.; Ke, X.; Zhong, L.; Zhao, H.; Ren, X. Understanding the mechanism of large dielectric response in Pb-free $(1−x)Ba(Zr_{0.2}Ti_{0.8})O_3−x(Ba_{0.7}Ca_{0.3})TiO_3$ ferroelectric ceramics. *Acta Mater.* **2017**, *125*, 77–186. [CrossRef]
9. Xiang, X.D.; Sun, X.; Briceño, G.; Lou, Y.; Wang, K.A.; Chang, H.; Wallance-Freedman, W.G.; Chen, S.W.; Schultz, P.G. A combinatorial approach to materials discovery. *Science* **1995**, *268*, 1738–1740. [CrossRef]
10. Fukumura, T.; Ohtani, M.; Kawasaki, M.; Okimoto, Y.; Kageyama, T.; Koida, T.; Hasegawa, T.; Tokura, Y.; Koinuma, H. Rapid construction of a phase diagram of doped Mott insulators with a composition-spread approach. *Appl. Phys. Lett.* **2000**, *77*, 3426–3428. [CrossRef]
11. Chang, K.S.; Aronova, M.; Famodu, O.; Takeuchi, I.; Lofland, S.E.; Hattrick-Simpers, J.; Chang, H. Multimode quantitative scanning microwave microscopy of in situ grown epitaxial $Ba_{1−x}Sr_xTiO_3$ composition spreads. *Appl. Phys. Lett.* **2001**, *79*, 4411–4413. [CrossRef]
12. Christen, H.M.; Silliman, S.D.; Harshavardhan, K.S. Continuous compositional-spread technique based on pulsed-laser deposition and applied to the growth of epitaxial films. *Rev. Sci. Instrum.* **2001**, *72*, 2673–2678. [CrossRef]
13. Koinuma, H.; Takeuchi, I. Combinatorial solid-state chemistry of inorganic materials. *Nat. Mater.* **2004**, *3*, 429–438.
14. Venimadhav, A.; Yates, K.A.; Blamire, M.G. Scanning Raman spectroscopy for characterizing compositionally spread films. *J. Comb. Chem.* **2005**, *7*, 85–89. [CrossRef] [PubMed]
15. Qiu, J.; Liu, G.Z.; Wolfman, J.; Autret-Lambert, C.; Roger, S.; Gao, J. Structure and dielectric characteristics of continuous composition spread $Ba_{1−x}Sr_xTiO_3$ thin films by combinatorial pulsed laser deposition. *Ceram. Int.* **2016**, *42*, 6408–6412. [CrossRef]
16. Jaber, N.; Wolfman, J.; Daumont, C.; Négulescu, B.; Ruyter, A.; Feuillard, G.; Bavencoffe, M.; Fortineau, J.; Sauvage, T.; Courtois, B.; et al. Enhancement of piezoelectric response in Ga doped $BiFeO_3$ epitaxial thin films. *J. Appl. Phys.* **2015**, *117*, 244107. [CrossRef]
17. Nagata, T.; Kumaragurubaran, S.; Suzuki, Y.; Takahashi, K.; Ri, S.G.; Tsunekawa, Y.; Suzuki, S.; Chikyow, T. Combinatorial thin film synthesis for developments of new high dielectric constant thin film materials. *Trans. Mat. Res. Soc. Jpn.* **2018**, *43*, 249–254. [CrossRef]
18. Hussey, B.W.; Gupta, A. Synthesis of $YBa_2Cu_3O_{7−\delta}$ films from separate oxide targets. *J. Appl. Phys.* **1992**, *72*, 287–289. [CrossRef]
19. Ito, A.; Machida, A.; Obara, M. Cobalt doping in $BaTiO_3$ thin films by two-target pulsed KrF laser ablation with in situ laser annealing. *Appl. Phys. Lett.* **1997**, *70*, 3338–3340. [CrossRef]
20. Schenck, P.K.; Kaiser, D.L.; Davydov, A.V. High throughput characterization of the optical properties of compositionally graded combinatorial films. *Appl. Surf. Sci.* **2004**, *223*, 200–205. [CrossRef]

21. Keller, D.A.; Ginsburg, A.; Barad, H.-N.; Shimanovich, K.; Bouhadana, Y.; Rosh-Hodesh, E.; Takeuchi, I.; Aviv, H.; Tischler, Y.R.; Anderson, A.Y.; et al. Utilizing pulsed laser deposition lateral inhomogeneity as a tool in combinatorial material science. *ACS Comb. Sci.* **2015**, *17*, 209–216. [CrossRef]

22. Itina, T.E.; Marine, W.; Autric, M. Monte Carlo simulation of pulsed laser ablation from two-component target into diluted ambient gas. *J. Appl. Phys.* **1997**, *82*, 3536–3542. [CrossRef]

23. Saenger, K.L. *Pulsed Laser Deposition of Thin Films*; Chrisey, D.B., Hubler, G.K., Eds.; Wiley: New York, NY, USA, 1994; pp. 199–227.

24. Singh, R.K. Spatial thickness variations in laser-deposited thin films. *Mater. Sci. Eng. B* **1997**, *45*, 180–185. [CrossRef]

25. Rashidian Vaziri, M.R.; Hajiesmaeilbaigi, F.; Maleki, M.H. Monte Carlo simulation of the subsurface growth mode during pulsed laser deposition. *J. Appl. Phys.* **2011**, *110*, 043304. [CrossRef]

26. Urushibara, A.; Moritomo, Y.; Arima, T.; Asamitsu, A.; Kido, G.; Tokura, Y. Insulator-metal transition and giant magnetoresistance in $La_{1-x}Sr_xMnO_3$. *Phys. Rev. B* **1995**, *51*, 14103–14109. [CrossRef] [PubMed]

27. Coey, J.M.D.; Viret, M.; von Molnar, S. Mixed-valence manganites. *Adv. Phys.* **1999**, *48*, 167–293. [CrossRef]

28. Bond, W.L. Notes on solution of problems in odd job vapor coating. *J. Opt. Soc. Am.* **1954**, *44*, 429–438. [CrossRef]

29. Bassim, N.D.; Schenck, P.K.; Otani, M.; Oguchi, H. Model, prediction, and experimental verification of compositionand thickness in continuous spread thin film combinatorial libraries grown by pulsed laser deposition. *Rev. Sci. Instr.* **2007**, *78*, 072203. [CrossRef]

30. Shirane, G.; Suzuki, K. Crystal structure of Pb(Zr-Ti)O_3. *J. Phys. Soc. Jpn.* **1952**, *7*, 333. [CrossRef]

31. Foster, C.M.; Bai, G.-R.; Csencsits, R.; Vetrone, J.; Jammy, R.; Wills, L.A.; Carr, E.; Amano, J. Single-crystal $Pb(Zr_xTi_{1-x})O_3$ thin films prepared by metal-organic chemical vapor deposition: Systematic compositional variation of electronic and optical properties. *J. Appl. Phys.* **1997**, *81*, 2349–2357. [CrossRef]

32. Wiedenhorst, B.; Höfener, C.; Lu, Y.; Klein, J.; Alff, L.; Gross, R.; Freitag, B.H.; Mader, W. Strain effects and microstructure of epitaxial manganite thin films and heterostructures. *Appl. Phys. Lett.* **1999**, *74*, 3636–3638. [CrossRef]

33. Wu, W.; Wong, K.H.; Choy, C.L.; Zhang, Y.H. Top-interface-controlled fatigue of epitaxial $Pb(Zr_{0.52}Ti_{0.48})O_3$ ferroelectric thin films on $La_{0.7}Sr_{0.3}MnO_3$ electrodes. *Appl. Phys. Lett.* **2000**, *77*, 3441–3443. [CrossRef]

34. Konishi, Y.; Fang, Z.; Izumi, M.; Manako, T.; Kasai, M.; Kuwahara, H.; Kawasaki, M.; Terakura, K.; Tokura, Y. Orbital-state-mediated phase-control of manganites. *J. Phys. Soc. Jpn.* **1999**, *68*, 3790–3793. [CrossRef]

35. Song, J.H.; Susaki, T.; Hwang, H.Y. Enhanced thermodynamic stability of epitaxial oxide thin films. *Adv. Mater.* **2008**, *20*, 2528–2532. [CrossRef]

36. Roqueta, J.; Pomar, A.; Balcells, L.; Frontera, C.; Valencia, S.; Abrudan, R.; Bozzo, B.; Konstantinović, Z.; Santiso, J.; Martínez, B. Strain-engineered ferromagnetism in LaMnO$_3$ thin films. *Cryst. Growth Des.* **2015**, *15*, 5332–5337. [CrossRef]